Three-dimensional MHD simulation of the evolution of the April 2000 CME event and its induced shocks using a magnetized plasma blob model

F. Shen,[1] X. S. Feng,[1] S. T. Wu,[2] C. Q. Xiang,[1] and W. B. Song[1]

Received 13 June 2010; revised 28 January 2011; accepted 1 February 2011; published 1 April 2011.

[1] A three-dimensional (3-D) time-dependent, numerical magnetohydrodynamic (MHD) model with asynchronous and parallel time-marching method is used to investigate the propagation of coronal mass ejections (CMEs) in the nonhomogenous background solar wind flow. The background solar wind is constructed based on the self-consistent source surface with observed line-of-sight of magnetic field and density from the source surface of 2.5 R_s to the Earth's orbit (215 R_s) and beyond. The CMEs are simulated by means of a very simple flux rope model: a high-density, high-velocity, and high-temperature magnetized plasma blob is superimposed on a steady state background solar wind with an initial launch direction. The dynamical interaction of a CME with the background solar wind flow between 2.5 and 220 R_s is investigated. The evolution of the physical parameters at the cobpoint, which is located at the shock front region magnetically connected to ACE spacecraft, is also investigated. We have chosen the well-defined halo-CME event of 4–6 April 2000 as a test case. In this validation study we find that this 3-D MHD model, with the asynchronous and parallel time-marching method, the self-consistent source surface as initial boundary conditions, and the simple flux rope as CME model, provide a relatively satisfactory comparison with the ACE spacecraft observations at the L1 point.

Citation: Shen, F., X. S. Feng, S. T. Wu, C. Q. Xiang, and W. B. Song (2011), Three-dimensional MHD simulation of the evolution of the April 2000 CME event and its induced shocks using a magnetized plasma blob model, *J. Geophys. Res.*, *116*, A04102, doi:10.1029/2010JA015809.

1. Introduction

[2] Corona mass ejections (CMEs) and their interplanetary consequences (ICMEs) represent different aspects of the same phenomenon responsible for large non-recurrent geomagnetic storms [*Gosling*, 1990]. Because of their great complexity, each aspect has typically been investigated separately, which is useful for revealing the basic underlying physics. However, in order to obtain a complete picture, one needs to conduct 3-D magnetohydrodynamic (MHD) modeling to consider the coupling between the corona and the interplanetary processes.

[3] In the past 10 years, a large amount of work has been done in numerical studies of CMEs and their interplanetary manifestations. Here, we have no intension of giving a review about the numerical progress in 3-D MHD simulation of these features. The following description is limited only to those closely related to our present study. In simulating the large-scale solar wind and its interaction with CMEs, regional combination method of linking the coronal model (in subsonic/sub-Alfvénic to supersonic/super-Alfvénic region) and the inner heliospheric model (in supersonic/super-Alfvénic region) is usually used in order to provide a fast convergence as well as save computer time. Successful merging of two-dimensional and three-dimensional (2-D and 3-D) MHD coronal and heliospheric models has been performed and reviewed [*Wu et al.*, 1997, 1999; *Odstrcil et al.*, 2002]. *Usmanov et al.* [2000] used a global axisymmetric MHD solar wind model with WKB Alfvén waves, by combining a time relaxation numerical technique in the 2-D solar corona region (1–22 R_s) with a marching-along-radius method in the outer region (22 R_s–10 AU). The large-scale structure of solar wind was also simulated by *Feng et al.* [2005] and *Shen et al.* [2007] by using the 3-D MHD regional combination numerical model (hereafter called Corona-interplanetary total variation diminishing (TVD) MHD model, COIN-TVD model for brevity). In the COIN-TVD model, the 3-D MHD equations were solved by combining a time relaxation numerical technique in the corona with a marching-along-radius method in the heliosphere. Afterward, in order to improve the precision in the heliosphere and save computational cost, *Shen et al.* [2009] made a

[1]SIGMA Weather Group, State Key Laboratory of Space Weather, Center for Space Science and Applied Research, Chinese Academy of Sciences, Beijing, China.
[2]Center for Space Plasma and Aeronomic Research, University of Alabama in Huntsville, Huntsville, Alabama, USA.

0148-0227/11/2010JA015809

modification to the 3-D COIN-TVD model, which incorporated the whole time-dependent simulation from the solar surface to 1 AU by applying an asynchronous and parallel time-marching method during the simulation. The solar wind governing equations are characterized by the initial boundary value problem of the MHD system. The initial boundary conditions control the solar wind structures. Currently, the observed photospheric magnetic field constraint and Parker's solar wind solution are usually used as inputs to the MHD models [e.g., *Riley et al.*, 2001; *Linker et al.*, 1999; *Odstrcil et al.*, 2003, 2004, 2005; *Hayashi*, 2005; *Owens et al.*, 2008; *Shen et al.*, 2009]. In order to obtain more realistic solar wind background, more observational data constraints are needed. To this effort, our modified 3-D COIN-TVD model employs the self-consistent structures on the source surface as the initial boundary conditions, which is derived from the observation of the solar magnetic field and K-coronal brightness with the help of MHD equations at 2.5 R_s according to the global distribution of coronal mass output's flux F_m (= density n × speed v) [*Wei et al.*, 2003; *Shen et al.*, 2007, 2010].

[4] Presently, the mechanism of CME generation is unclear. Alternatively, simple generation models for CMEs often work well for CME shock evolution studies, which consist in a big pressure or velocity value at the inner boundary. *Jacobs et al.* [2005] superimposed a CME on their 2.5-D MHD solar wind solution where they used a simple "density (+pressure)-driven" model and simulated CMEs both in the equatorial streamer belt and at larger latitudes. *Groth et al.* [2000] also simulated "density-driven" CMEs superimposed on a 3-D ideal MHD solar wind solution and studied their interaction with the magnetosphere-ionosphere system. Then, the "pressure-driven model" model was used in the numerical simulation by many authors [*Odstrcil et al.*, 2004, 2005; *Plunkett and Wu*, 2000; *Shen et al.*, 2007, 2009; *Zhou et al.*, 2008].

[5] In recent years, to reproduce the magnetic field evolution of the CME more clearly, many authors chose the preexisting flux rope model as CME initiation. A preexisting flux rope can be superposed out of equilibrium to the steady state surface. *Roussev et al.* [2003] used the loss of equilibrium of the *Titov and Démoulin* [1999] flux rope model as CME initiation, although the evolution of this CME is only simulated in the lower corona. *Manchester et al.* [2004a, 2004b] used an analytical 3-D self-similar flux rope [*Gibson and Low*, 1998] in the streamer belt to mimic the CME and followed its evolution up to 32 R_s and to 336 R_s. The model of *Manchester et al.* [2004a, 2004b] adopted the flux rope geometry and the MHD forces driving it, which was essentially the concept proposed by *Chen* [1996]. This model purports to calculate the forces acting on CMEs and CME expansion from the Sun through the heliosphere.

[6] In some space weather event simulations, the evolutionary properties of the CME are usually determined by the simulations with verification by the ACE data at L1 point. *Krall et al.* [2006] determined the best fit parameters for the 28 October 2003 event, by using the modified erupting flux rope (EFR) model, in which the CME dynamics and the magnetic field evolution were determined by a set of coupled equations representing the toroidal hoop force with momentum coupling to the ambient solar wind via drag [*Chen*, 1989, 1996; *Chen and Garren*, 1993; *Krall et al.*, 2000]. Recently, by using the EFR model and applying minimum-D solutions [*Chen and Kunkel*, 2010], *Kunkel and Chen* [2010] determined the best-fit parameters for the 24 December 2007 event. *Chané et al.* [2005, 2006, 2008] used a 2.5-D axisymmetric CME model to superimpose a high-density, high-velocity magnetized plasma blob on the background solar wind, and *Chané et al.* [2008] also discussed how to combine the ACE data with the numerical simulations to determine the initial characteristics of the halo CME, observed on 4 April 2000.

[7] Presently, all these CME models are candidates for mimicking the morphology near the Sun, with the purpose of reproducing the plasma parameters comparable with 1 AU observation. For example, the "pressure-driven" models, which belong to non flux rope models, have the simplest type and are suitable for the CME shock evolution studies, while because these models do not use a magnetized ejecta, they often could not well provide the magnetic field structure of the CME and the change in speed of a shock wave inside a magnetic cloud, as mentioned by *Lugaz and Roussev* [2010]. The GL flux rope model [*Gibson and Low*, 1998; *Manchester et al.*, 2004a, 2004b] can approach the basic features of the canonical three-part density structure (front-cavity-core) and capturing the early coherent phase of CME evolution. The magnetized plasma blob model given by *Chané et al.* [2005, 2006, 2008] is a kind of very simple flux rope model for CME initiation, which has relative simple type and can reproduce some features about the magnetic cloud; moreover, the best fit parameters of the CME initial state can be determined to get a relative close comparison with the ACE data at L1 point.

[8] In the present paper, we present a 3-D solar wind background MHD model with self-consistent source surface structures as initial boundary conditions [*Shen et al.*, 2007], which is derived from the observation of the solar magnetic field and K-coronal brightness [*Wei et al.*, 2003]. A high-density, high-velocity, and high-temperature magnetized plasma blob model is used for the initiation of the CME observed by SOHO/LASCO on 4 April 2000, which is similar to the plasma blob model given by *Chané et al.* [2005, 2006, 2008], in order to reproduce the in situ data obtained by the ACE spacecraft for the halo CME event of 4 April 2000. This is done by adjusting the CME initial parameters (density, magnetic field strength, velocity, temperature) of the plasma blob in the numerical simulation model to yield the best possible fit with the ACE data. The simulated background solar wind is presented in section 2 and the simulation of 4–6 April 2000 CME event and its induced shock's characteristics are given in section 3. Finally, the summary and concluding remarks are given in section 4.

2. Three-Dimensional MHD Simulation of Solar Wind Background for CR 1961

[9] Here the 3-D MHD simulation of background solar wind for CR 1961 is presented, with self-consistent source surface structures as the initial boundary condition. The computational domain for this 3-D MHD simulation is a Sun-centered spherical coordinate system (r, θ, φ) with the r axis in the ecliptic plane. The Earth (L1 point) is located at r = 215 R_s (213 R_s), θ = 0°, and φ = 180°.

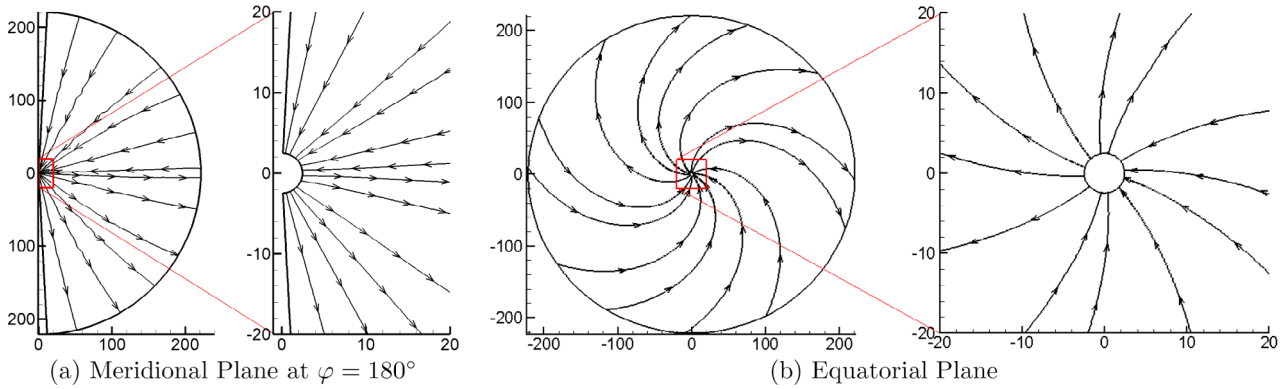

Figure 1. The calculated steady state solution for the magnetic field in (a) the meridional plane at φ = 180° and (b) the equatorial plane from 2.5 to 220 R_s and at smaller scale at 100 h (unit of the axis: R_s).

The computational domain covers 2.5 $R_s \le r \le$ 220 R_s; $-89° \le \theta \le 89°$ and $0° \le \varphi \le 360°$. The grid mesh is chosen to be 394(r) × 89(θ) × 180 (φ). The grid size is uniform in azimuth, with $\Delta\varphi = 2°$. The radial grid (r_i) and meridional grid (θ_j) are not uniform. In order to obtain a precise computational resolution, we choose for the radial grid: $r(1) = 2.5$ R_s, $\Delta r(1) = s \times$ r(1), $r(i) = r(i-1) + \Delta r(i-1)$, Δr(i) = $s \times$ r($i-1$), where $s = \pi/200$ ($\pi = 3.1415926$) between 2.5 R_s and 22 R_s and $s = \pi/260$ between 22 R_s and 220 R_s. The spatial resolution in the radial direction gradually varies from ~0.03 Rs at the inner boundary of 2.5 Rs to ~2.0 Rs near 1 AU at 215 Rs. For the meridional grid we choose $\Delta\theta$ (0°) = 1.0°, $\Delta\theta$ (−89°) = $\Delta\theta$ (89°) = 3.0°, with a constant increase in $\Delta\theta$ from θ = 0° to θ = ±89°.

[10] The numerical 3-D MHD scheme used in this paper is a modified Total Variation Diminishing/Lax-Friedrichs (TVD/LF) type scheme [*Feng et al.*, 2003, 2005; *Shen et al.*, 2007, 2009] with electric field modification method [*Tóth*, 2000] for the assurance of $\nabla \bullet \vec{B} = 0$. Thus this numerical model satisfies $\nabla \bullet \vec{B} = 0$ to round-off error. This is achieved by the field-interpolated central difference approach for solving the magnetic field [*Tóth*, 2000].

[11] In the present paper, the time-dependent 3-D ideal MHD equations also include solar rotation and volumetric heating [*Shen et al.*, 2007], where the pressure equation and the volumetric heating function Q are given by

$$\frac{\partial p}{\partial t} + \frac{1}{r^2}\frac{\partial r^2(pv_r)}{\partial r} + \frac{1}{r\sin\theta}\frac{\partial \sin\theta(pv_\theta)}{\partial \theta} + \frac{1}{r\sin\theta}\frac{\partial (pv_\varphi)}{\partial \varphi} = -(\gamma-1)p\nabla \bullet \vec{v} + (\gamma-1)Q \quad (1)$$

where

$$Q = -\rho q_0 (T - T_0)\exp\left[-\frac{(r-R_s)^2}{\sigma_0^2}\right] \quad (2)$$

where T_0 and q_0 have the same meaning as that in the work of *Groth et al.* [2000]. $T_0(\theta = 0°) = 1.5 \times 10^6$ K, $T_0(\theta = \pm 89°) = 2.6 \times 10^6$ K, $\sigma_0 = 4.5$ R_s, and the meaning of other parameters can be found in our previous paper [*Shen et al.*, 2007].

[12] The self-consistent source surface distribution is used as the initial boundary conditions at 2.5 R_s [*Wei et al.*, 2003; *Shen et al.*, 2007, 2010]. The initial conditions of density (ρ) and magnetic field (B_r, B_θ, B_φ) can be deduced from the observed K-coronal brightness and photospheric magnetic field (B_r) with potential field model for CR 1961 according to an observation-based model of the background solar wind [*Xiang et al.*, 2006; *Shen et al.*, 2007, 2010], and the initial four parameters for v_r, v_θ, v_φ, and T can be computed based on the initial density distribution and the self-consistent initial boundary conditions at the inner boundary [*Shen et al.*, 2007, 2010].

[13] In order to reasonably accommodate the source surface distribution into our MHD model, the method of projected characteristics [*Nakagawa et al.*, 1987; *Wu and Wang*, 1987; *Hayashi*, 2005; *Wu et al.*, 2006] is employed at the lower boundary (2.5 R_s). For the details about the method of projected characteristics, refer to the Appendix of *Wu et al.* [2006]. At the outer boundary of 220 R_s, we employ a linear extrapolation. Because the solar wind is supersonic/Alfvénic at the outer boundary, this treatment is equivalent to a nonreflecting boundary.

[14] To save computation time and maintain simulation accuracy, we use the asynchronous and parallel time-marching method by using different local time steps (adapted to the local CFL condition) in the corona (2.5 R_s to 22 R_s) and the heliosphere (22 R_s to 220 R_s) and applying parallel computation in the r direction for this simulation [*Shen et al.*, 2009]. The simulation time of the background solar wind using the asynchronous method is <1/6 of that using the normal synchronous time-marching method without any influence on computation precision.

[15] The calculated steady state magnetic field lines in the meridional plane at φ = 180° (Figure 1a) and equatorial plane (Figure 1b) are shown in Figure 1. The 3-D magnetic field topology and radial velocity distribution are shown in Figure 2. It takes ~100 h to reach the MHD equilibrium state. The well-known Archimedes' spiral lines are reproduced in Figure 1b and Figure 2.

[16] Figure 3 shows the distribution of B_r, n, T, and V_r in the corona (r = 22 R_s) and the heliosphere (r = 215 R_s) based on the asynchronous time-marching method. Profiles of the radial magnetic field (B_r), proton number density (n), temperature (T), and the radial velocity (v_r) at r = 22 R_s (corona) and r = 215 R_s (heliosphere) (meridional profiles at

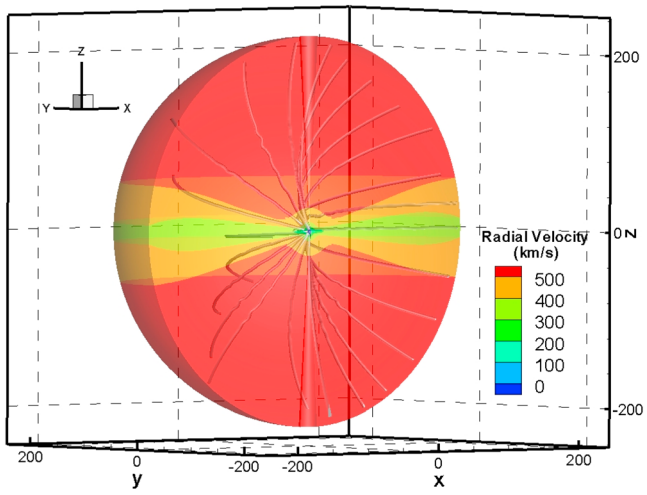

Figure 2. The calculated steady state 3-D magnetic field lines and radial velocity distribution, from 2.5 to 220 R_s at 100 h (unit of the axis: R_s).

$\varphi = 180°$) are shown in Figure 3 (left) and Figure 3 (right), respectively. Both the configurations of the corona and the heliosphere consist of a dense, low-temperature, and slow flow near the current sheet. The sign of the radial magnetic fields are different at the two sides of the current sheet, both in the corona and the heliosphere. These simulated features about the heliosphere are consistent with the Ulysses observation [*McComas et al.*, 2000, 2003, 2006]. Further, we have compared the present solar wind simulation with Helios 2 data from 0.3 AU to 1 AU shown in Figure 4. The Helios 2 data were measured between 20 March (day of year (DOY) 80) 1976 and 28 June (DOY 180) 1976, when the spacecraft was situated between 0.3 and 1 AU from the Sun. The spacecraft trajectories of Helios 2 as projected on the ecliptic plane were shown in Figure 1 of *Mariani et al.* [1979] for periods of interest: the heliographic latitude of the spacecraft was always in the range ±7.23° [*Mariani et al.*, 1979]. Figure 4a (top) shows the heliocentric distance of Helios 2 changing with the DOY of 1976. Figure 4a also gives the total magnetic field (nT), plasma density (cm^{-3}), and plasma temperature (k) of Helios 2 when it moved between 0.3 and 1 AU. Figure 4b plots the total magnetic field (nT), plasma density (cm^{-3}), and temperature (k) of our simulation at the corresponding position of Helios 2 in Figure 4a. These solar wind parameters of the simulated and measured profiles are similar for the decreasing tendency as a whole; the general shape of the curves is reproduced successfully.

3. Numerical Simulation of 4–6 April 2000 CME Event

3.1. CME Initiation

[17] Detailed descriptions of the 4–6 April 2000 event have been reported by a number of authors [*Huttunen et al.*, 2002; *Jadav et al.*, 2005; *Chané et al.*, 2006, 2008; *Aran*, 2007; *Rodríguez et al.*, 2009]. For completeness we will summarize some of the highlights for this event.

[18] The full halo CME was first seen in the LASCO C2 field of view on 4 April 2000 at 1632 UT. The projected speed according to the LASCO CME catalog is 1188 km/s. A C9.7 flare peaking at 1512 UT was detected accompanying this event, located at N16W66. The CME arrived at the L1 point (1.5×10^9 m from the Earth to sunward) on 6 April 2000 at 1604 UT based on the ACE spacecraft observation, followed by a very long sheath region from 1600 UT until 0900 UT on the following day which shows that the interplanetary disturbance caused by this CME takes about 47.5 h to reach the L1 point. This CME produced the second strongest magnetic storm in the year 2000 (Dst value of −228 nT). This was the strongest magnetic storm since November 1991 and one of the seven largest magnetic storms in the history of Dst measurements [*Jadav et al.*, 2005].

[19] To simulate this CME event, a high-density, high-velocity, and high-temperature magnetized plasma blob is superimposed on the background solar wind model. The CME is launched at a certain velocity in a given direction and are further characterized by a given density, radial velocity, temperature, magnetic field strength, and magnetic polarity. The initial CME magnetic field and the background wind magnetic field can have the same or the opposite polarity. It can be called as an inverse and a normal CME, respectively, as described by *Chané et al.* [2005, 2006].

[20] The density, radial velocity, and temperature profile of the initial perturbation are defined as follows:

$$\begin{cases} \rho_{CME}(r,\theta,\varphi) = \dfrac{\rho_{\max}}{2}\left(1-\cos\left(\pi\dfrac{a_{cme}-a(r,\theta,\varphi)}{a_{cme}}\right)\right) \\ V_{CME}(r,\theta,\varphi) = \dfrac{v_{\max}}{2}\left(1-\cos\left(\pi\dfrac{a_{cme}-a(r,\theta,\varphi)}{a_{cme}}\right)\right) \\ T_{CME}(r,\theta,\varphi) = \dfrac{T_{\max}}{2}\left(1-\cos\left(\pi\dfrac{a_{cme}-a(r,\theta,\varphi)}{a_{cme}}\right)\right) \end{cases} \quad (3)$$

where a_{cme} is the radius of the initial plasma blob, $a(r, \theta, \varphi)$ denotes the distance from the center of the initial plasma blob, and $\rho_{\max}$, $v_{\max}$, and $T_{\max}$ are the maximum density, radial velocity, and temperature in the plasma bubble added on top of the background solar wind, respectively.

[21] For the initial magnetic field of the CME model, *Chané et al.* [2005, 2006, 2008] prescribed the structure of the poloidal components B_R and B_Z in their 2.5-D cylindrical coordinate system, to quantify the effect of the initial magnetic field polarity on the evolution of the ICME. Here, in our 3-D spherical coordinate system, we present the radial and meridional components B_r and B_θ profile of the initial perturbation by means of a magnetic flux ψ. The initial magnetic field of the perturbation is defined as

$$\begin{cases} B_{r_{CME}}(r,\theta,\varphi) = -\dfrac{1}{r^2\sin\theta}\dfrac{\partial\psi(r,\theta,\varphi)}{\partial\theta} \\ B_{\theta_{CME}}(r,\theta,\varphi) = \dfrac{1}{r\sin\theta}\dfrac{\partial\psi(r,\theta,\varphi)}{\partial r} \end{cases} \quad (4)$$

where

$$\psi(r,\theta,\varphi) = \psi_0\left(a(r,\theta,\varphi) - \frac{a_{CME}}{2\pi}\sin\left(\frac{2\pi a(r,\theta,\varphi)}{a_{CME}}\right)\right) \quad (5)$$

is the magnetic flux function.

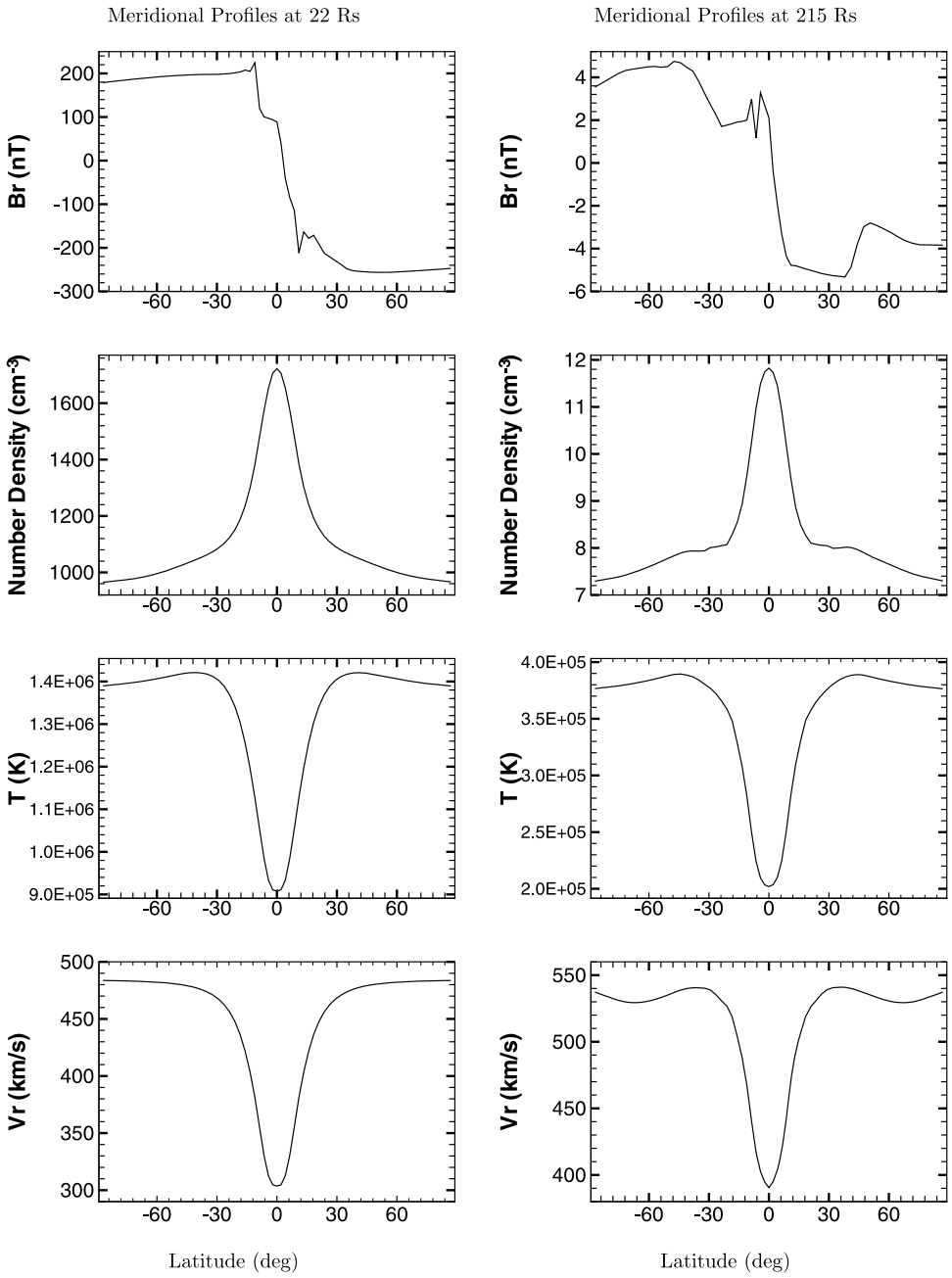

Figure 3. Profiles of the radial magnetic field, proton number density, temperature, and radial velocity at (left) r = 22 R_s (corona) and (right) r = 215 R_s (heliosphere) (meridional profiles at $\varphi = 180°$).

[22] This initial perturbation will be given by the following relation:

$$\begin{cases} \rho = \rho_0 + \rho_{CME}(r,\theta,\varphi) \\ v_r = v_{r0} + V_{CME}(r,\theta,\varphi) \\ T = T_0 + T_{CME}(r,\theta,\varphi) \\ B_r = B_{r0} + B_{rCME}(r,\theta,\varphi) \\ B_\theta = B_{\theta 0} + B_{\theta CME}(r,\theta,\varphi) \end{cases} \quad (6)$$

where ρ_0, v_{r0}, T_0, B_{r0}, and $B_{\theta 0}$ are the background values of the density, radial velocity, temperature, magnetic field in radial direction, and magnetic field in meridional direction calculated in section 2.

[23] In our simulation, the center of the initial plasma blob is situated at 3.5 R_s and is launched in direction of θ_{cme} = 16°, and φ_{cme} = 246° (N16W66 event). Then, we set a_{cme} = 0.5 R_s, v_{max} = 2500 km/s, $\rho_{max} = 2 \times 10^9$ cm^{-3}, $T_{max} = 2 \times 10^7$K; ψ_0 to obtain the initial maximum magnetic field as $\sim 7 \times 10^5$ nT, with an inverse magnetic polarity.

[24] The choice of these parameters is given to match the transit time, the total magnetic field, and other ACE data as

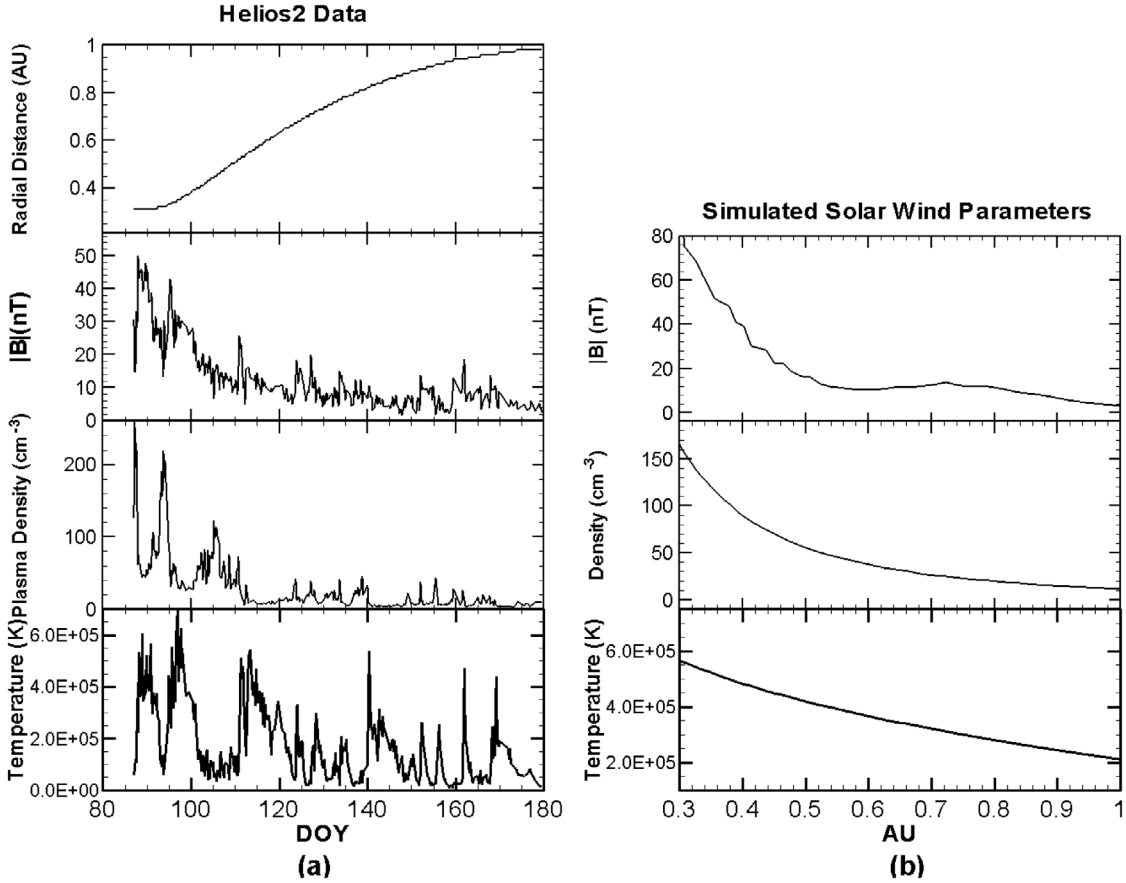

Figure 4. Comparison between (a) Helios 2 data and (b) our solar wind model from 0.3 to 1 AU. The Helios 2 data were measured between 20 March 1976 (DOY 80) and 28 June 1976 (DOY 180) when the spacecraft was situated between 0.3 and 1 AU from the Sun.

the best fit as possible. This initiation model will yield the driving force to launch a CME. *Wu et al.* [2004] made a detailed analysis about the driving mechanisms of the flux rope model. In their analysis, the injection of the magnetic flux can cause an additional Lorentz force to launch a CME, which was also mentioned by *Chen* [1996], and the introduction of the additional heating by raising the temperature of the flux rope also generates the driving force to launch a CME, since the pressure force is calculated from $p = \rho RT$.

[25] Figure 5 displays the 3-D intuitive views of the CME initialization on the background solar wind, which are the isosurfaces of the radial velocity v_r, (Figure 5a); total magnetic field |B| (Figure 5b); and x coordinate, y coordinate, and z coordinate magnetic field (B_x, B_y, and B_z) from Figures 5c to Figure 5e, respectively. In Figures 5a and 5b, the maximum value of the radial velocity and |B| appeared at the center of the initial plasma blob.

3.2. CME Simulation Results Compared With ACE Data and Dynamical Evolution

[26] Here the simulation results are presented. Figure 6 shows the profiles for the relative density $\left(\frac{\rho-\rho_o}{\rho_o}\right)$ at a constant longitude angle of $\varphi = 180°$ (Figure 6, top, the Earth location) and $\varphi = 246°$ (Figure 6, bottom, the CME's longitude). Figure 7 shows the relative density at a constant latitude angle: $\theta = 16°$ (Figure 7, top, the CME's heliolatitude), 0° (Figure 7, middle, equator, the Earth location), and $\theta = -16°$ (Figure 7, bottom). In Figure 6, the CME is shown to be much stronger and faster in the plane of longitude angle of 246° than that of 0° and in Figures 7, the CME is stronger and faster in the north than in the south. This is due to the fact that the source of CME was located at N16W66. From Figure 6e (top) and Figure 7e (middle), we notice that the CME arrival time to the L1 point is ~48 h, which is consistent with the observation of ACE.

[27] Figure 8 shows the propagation of the simulated CME at 15 min (Figure 8a), 1 h (Figure 8b), and 10 h (Figure 8c), respectively. Figure 8 (left) represents the relative density $\left(\frac{\rho-\rho_o}{\rho_o}\right)$ and magnetic field lines and its color code represents the three levels isosurfaces of density enhancement; Figure 8 (right) shows the higher spatial resolution of the magnetic topology of the simulated CME and its color code represents the magnitude of the radial velocity in units of kilometers per second. The magnetic field topology in Figure 8 is represented by the rod-shaped magenta lines. At time t = 15 min and t = 1 h, the flux rope are in the initial phase of the magnetic cloud (MC)-like structure of the flux rope that still has an almost circular shape, while at t = 10 h, the MC-like structure becomes obviously compressed. Figure 9 shows the detailed 3-D view of the CME in the corona and heliosphere

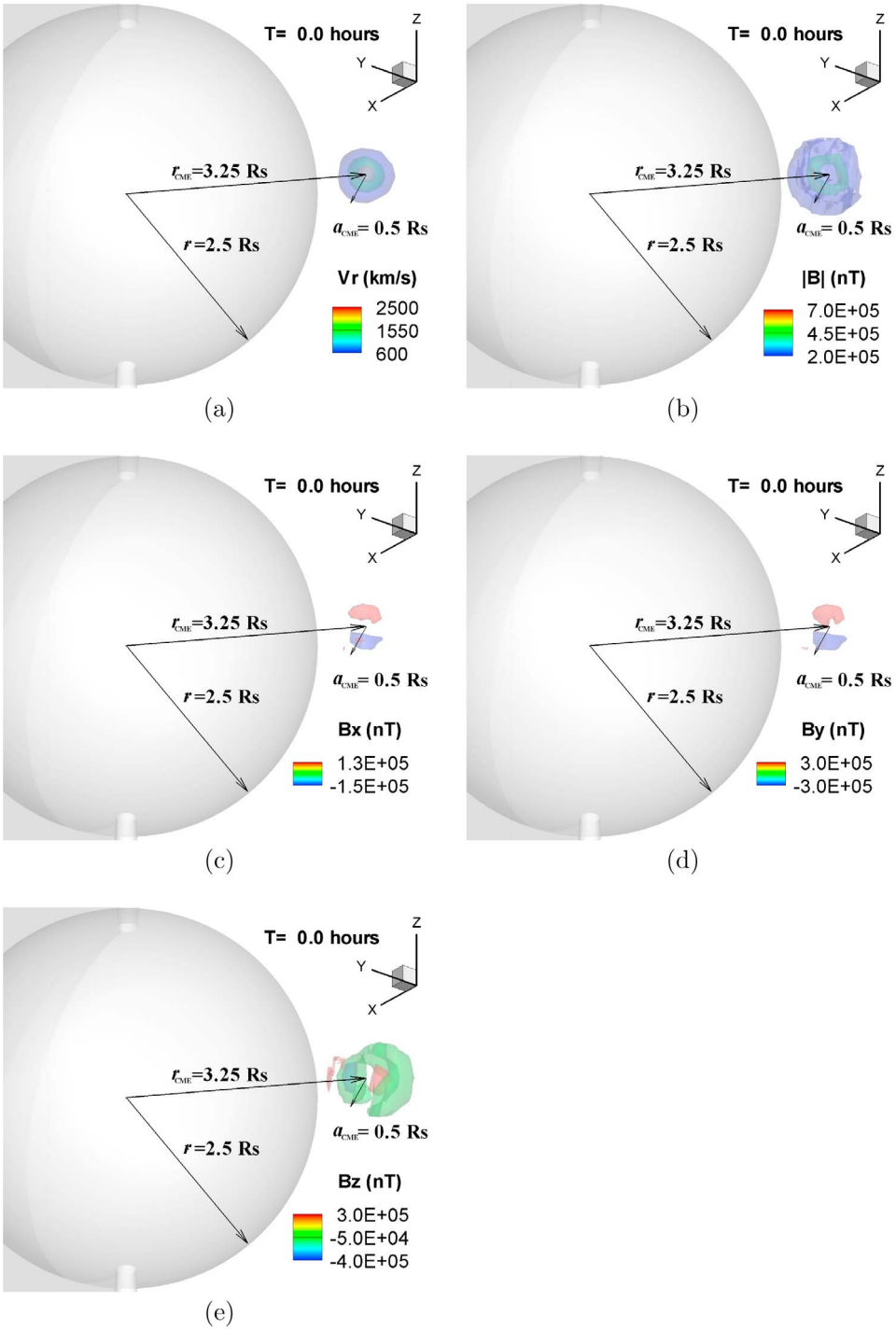

Figure 5. Three-dimensional views of the CME initialization, which are the isosurfaces of the (a) radial velocity (v_r), (b) total magnetic field ($|B|$), and (c–e) x, y, and z coordinate magnetic fields (B_x, B_y, and B_z).

at the later times of t = 20 h (Figure 9a), t = 30 h (Figure 9b), and t = 40 h (Figure 9c), in which the magnetic field is also represented by the rod-shaped magenta lines, and the radial velocity magnitude in units of kilometer per second is depicted by the false color image. The field outside of the flux rope region has the open field lines of the solar wind, some of which pass through the shock front where the lines bend sharply to wrap around the expanding flux rope. In the corona, the shock front is well defined both by the jump of the velocity and relative density, we recognize that the velocity has jumped from the ambient solar wind speed of 200–300 km/s to over 1000 km/s, and the relative density being a factor of 4–8, as shown in Figures 8a to 8c. In the heliosphere, the shock front is also defined by the jump of the velocity, which is from the ambient (~400–600 km/s) value to over 800 km/s value, as shown in Figures 9a to

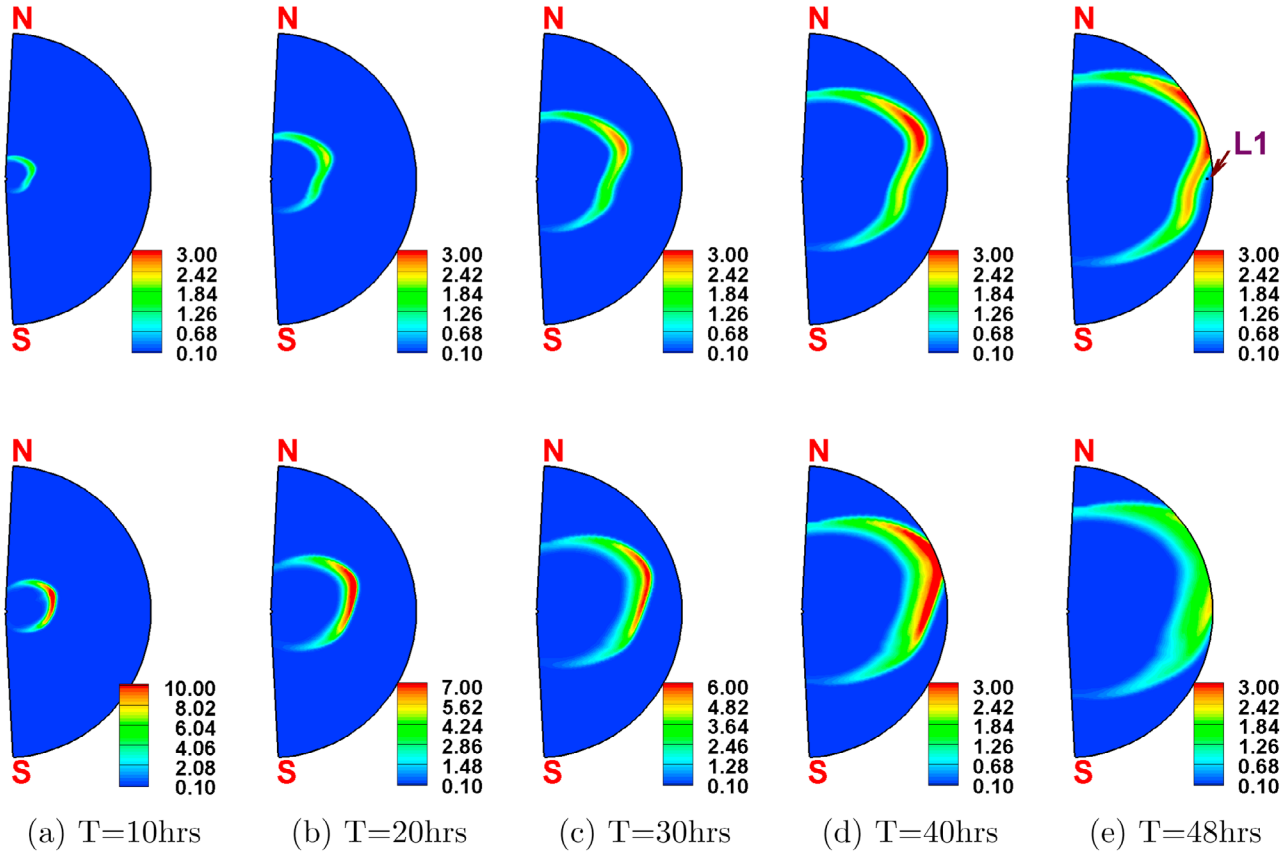

Figure 6. Evolution of the density contours $((\rho - \rho_0)/\rho_0)$ of the constant meridional angle of (top) φ = 180° and (bottom) φ = 246° at (a–e) five consecutive times (2.5–215 R_s).

9c. It shows that the shock is weakened because of the increasing of the ambient solar wind speed. The high-velocity (high-density) compression wave behind the shock is formed by the initial high-velocity (high-density) condition and the interactions between the plasma blob and the field.

[28] A shock front with a high velocity and relatively high density is clearly visible in Figures 6, 7, 8, and 9. The flux rope is radially compressed and a high plasma density builds up in front of flux rope. The distorted shock front is due to interaction with the slower solar wind around the heliospheric plasma sheets. The distortion is expected to be greater because of larger differences between slow and fast streams. This structural development is a consequence of the combined effects of (1) kinematic expansion, as the ejecta moves into an ever larger spherical volume, (2) dynamic evolution, as the ejecta plows into the slower ambient solar wind, and (3) the interaction between the lateral material expansion of the plasma blob and the background velocity and density of solar wind [*Odstrcil et al.*, 1996; *Odstrcil and Pizzo*, 1999a; *Dryer et al.*, 2001, 2004; *Odstrcil et al.*, 2003; *Riley et al.*, 2004]. North-south IMF components arise from shock compression, field line draping, and the ejected flux rope topology [*Detman et al.*, 1991; *Odstrcil and Pizzo*, 1999b]. Density and velocity enhancements trailing the flux rope (in the heliosphere) are signatures of the jetted outflow, driven by posteruptive reconnection underneath the flux rope (in the corona), as suggested by *Riley et al.* [2002].

[29] The results of our best attempt to fit the ACE data are shown in Figure 10. Figure 10 depicts the plots of total, x component, y component, z component magnetic field at the GSE coordinate system, number density, temperature, and velocity at the L1 point, respectively, from Figure 10 (top) to Figure 10 (bottom). Figure 10 describes the comparison of the computed plasma parameters with the ACE observed parameters. As it can be seen in Figure 10, in spite of the simple CME model used, our simulation has reproduced some of the in situ measurements; the general shape of the curves is similar, the radial velocity and temperature display realistic values, and the transit time is approximately reproduced. The leading shock, characterized by a sharp jump in the total magnetic field, number density, and velocity curves, arrives almost at the same time in the simulation with the in situ measurements. For the z component of the magnetic field, the simulated and measured profiles at the L1 point are similar, becoming southward first, then changing to northward, later changing to southward again, and finally tuning northward. However, there is a shift between the simulation and observation. To predict the intensity of a magnetic storm, the most important parameter is the z component of the magnetic field and this simulation does capture some realistic features. The solar wind speed is only indirectly important [*Wu and Lepping*, 2005]. We were able to reproduce these two parameters (B_z and V_r) quite well; our model may provide the potential as an additional

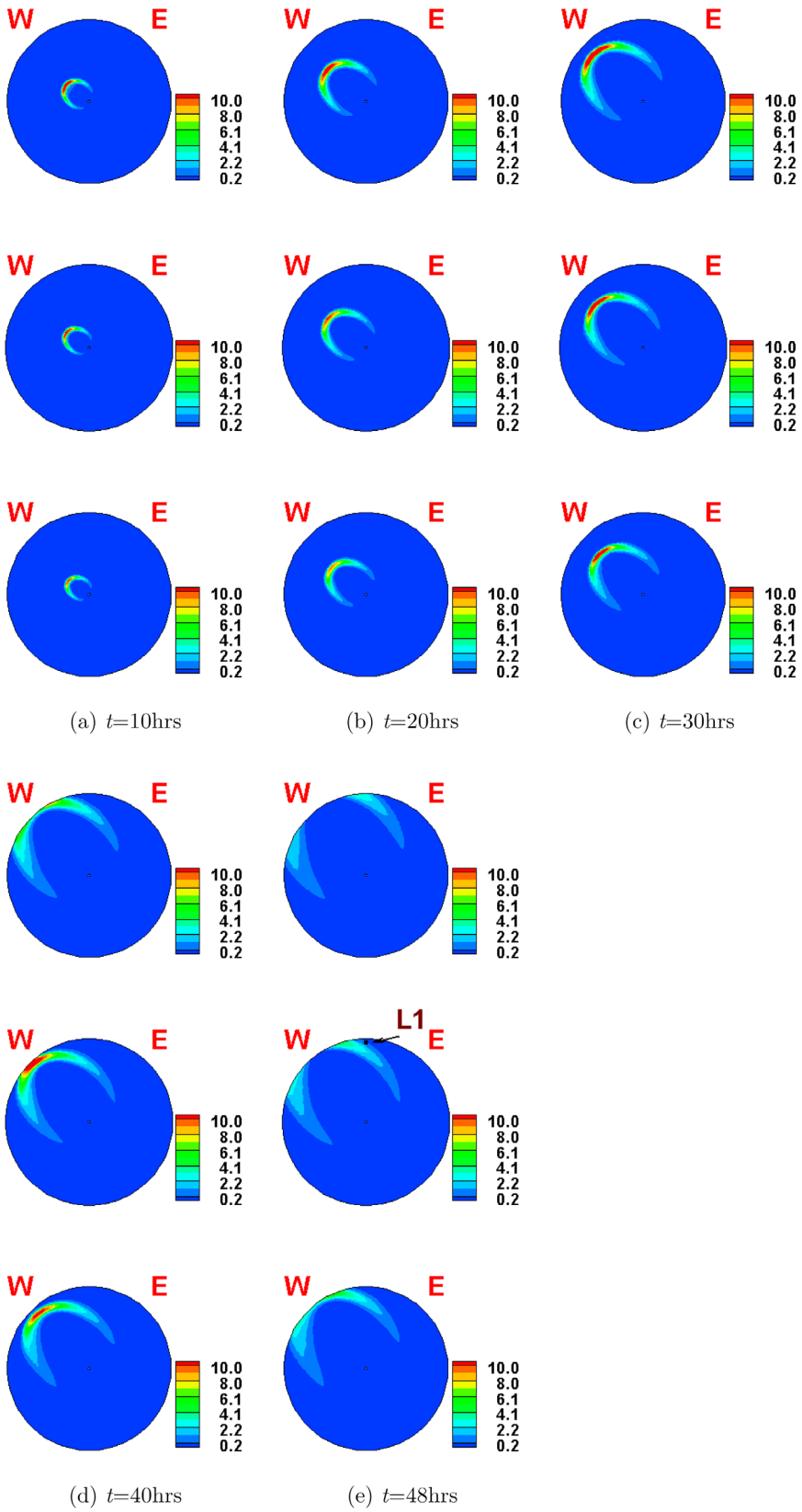

(a) t=10hrs (b) t=20hrs (c) t=30hrs

(d) t=40hrs (e) t=48hrs

Figure 7. Evolution of the density contours ($(\rho - \rho_0)/\rho_0$) of the constant latitude angle of (top) $\theta = 16°$, (middle) $\theta = 0°$, and (bottom) $\theta = -16°$ at (a–e) five consecutive times (2.5–215 R_s).

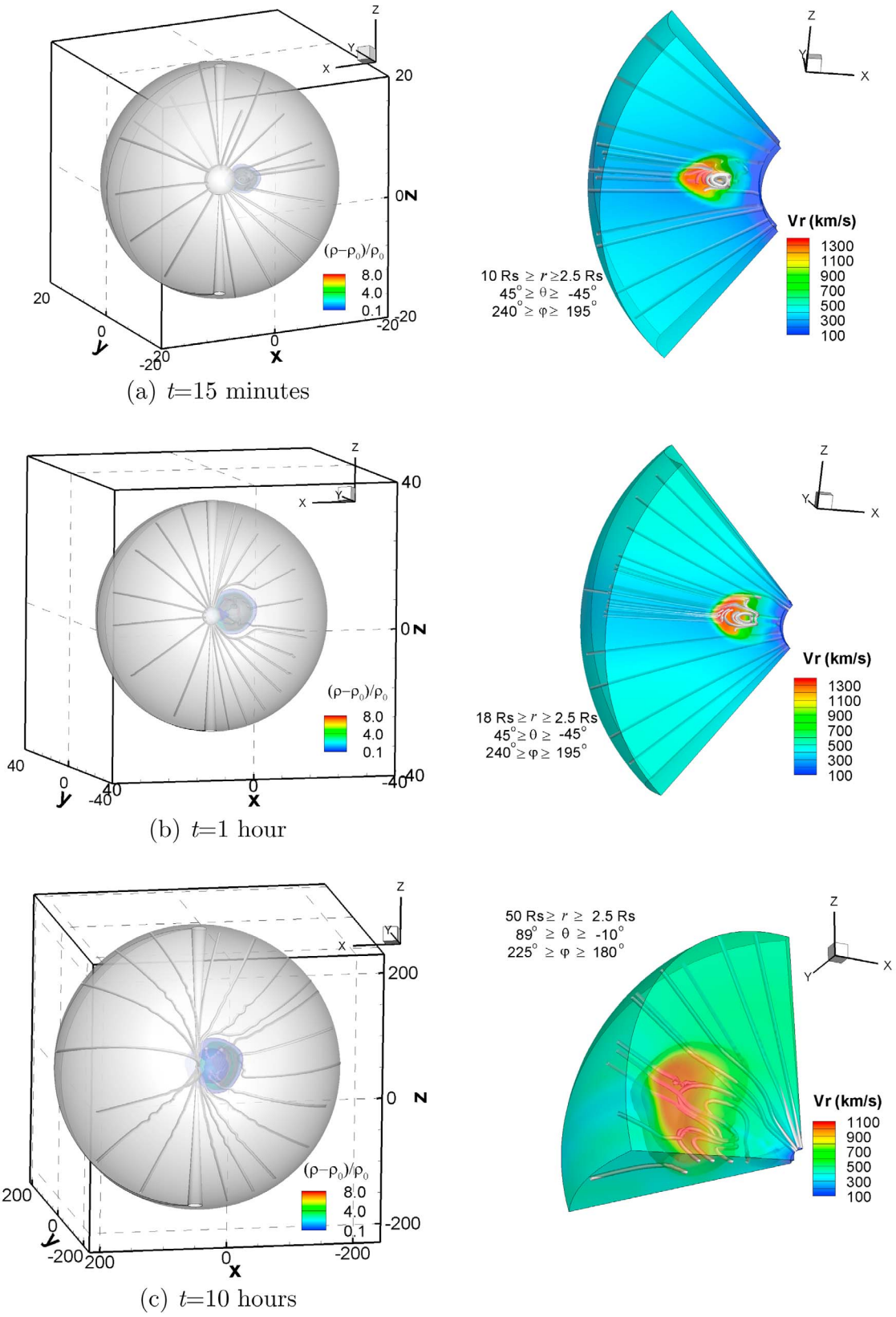

Figure 8. A three-dimensional representation of the CME shown (a) 15 min, (b) 1 h, and (c) 10 h after initiation. The solid rod-shaped lines are magnetic field lines, and the color codes represent (left) the relative density ($(\rho - \rho_0)/\rho_0$) isosurfaces and (right) the radial velocity magnitude (unit of the axis: R_s).

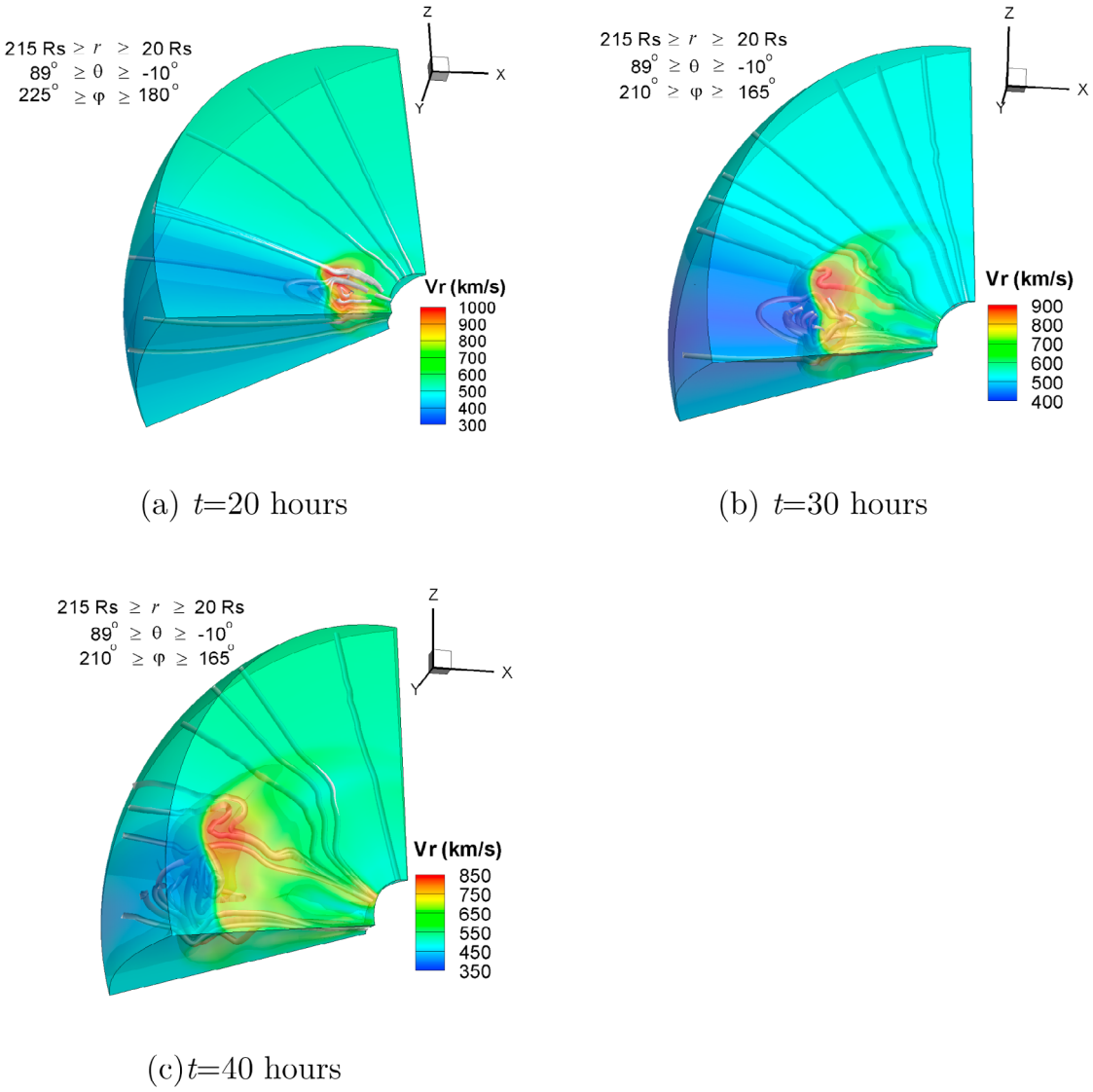

Figure 9. A three-dimensional representation of the CME shown (a) 20 h, (b) 30 h, and (c) 40 h after initiation. The solid rod-shaped lines are magnetic field lines, and the color codes represent the radial velocity magnitude (unit of the axis: R_s).

tool for predictions of the geoeffectiveness of IP CMEs. These results are also in agreement with those of the 2.5-D MHD model given by *Chané et al.* [2006, 2008].

[30] In Figure 10, we mark the simulated shock front with the red vertical solid line, which is caused by the leading edge of the flux rope. The beginning and ending of the simulated MC-like structure are also marked with two red vertical long-dashed lines. It should be pointed out that because the simulated structure of the ICME is hotter and denser than the background solar wind, it may not be appropriate to refer to this ICME as a magnetic cloud [*Burlaga et al.*, 1981; *Burlaga*, 1988]. Nevertheless, the ICME is cloudlike in other respects, with a smoothly rotating flux rope field structure and a relatively high speed. Therefore in the context we call this structure as the magnetic cloud (MC)-like structure.

[31] Some quantitative agreement is not expected in our simulation. The leading shock characterized by a jump in the velocity arrives ~1.5 h too early in the simulation. The maximum values of the temperature and the radial speed in the simulation are ~25% smaller and ~15% larger than the ACE data, respectively. For the z component of the magnetic field, the MC-like structure in our simulation seems to arrive ~1.5 h earlier than the ACE data and is also smaller than the observed magnetic cloud, especially for the southward magnetic field. Moreover, it should be pointed out that during the CME simulation, the grid is quite coarse, especially near 1 AU. The shock can be recognized within 2–3 grids, so in Figure 10, the simulated shock jump is much wider than the measured one.

[32] A number of CME events have been studied by using non-flux-rope models [*Odstrcil et al.*, 2004, 2005; *Shen et al.*, 2007, 2009; *Zhou et al.*, 2008] or by using preexisted flux rope models [*Manchester et al.*, 2004a, 2004b; *Kunkel and Chen*, 2010]. For different models, the comparability of the plasma parameters is different. *Odstrcil et al.* [2004,

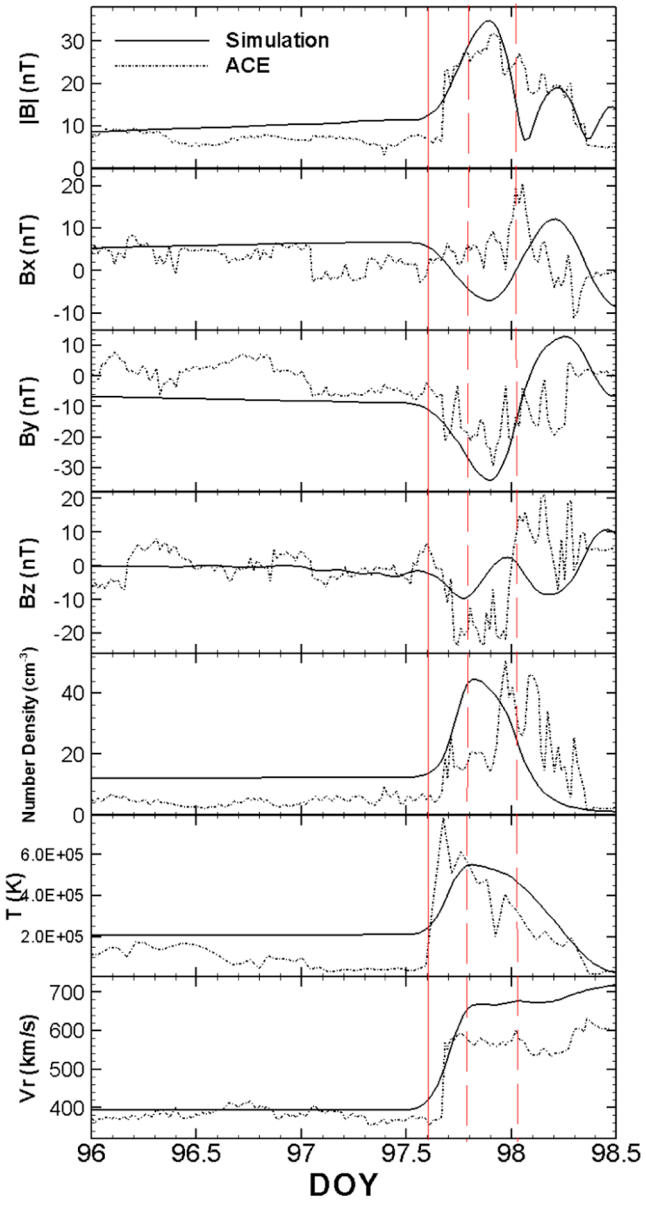

Figure 10. A comparison of the MHD simulation of the magnetic field and plasma parameters using the measured (ACE spacecraft) magnetic field and solar wind parameters at L1 point in 2000. The solid lines denote simulation parameters: (top to bottom) the magnetic field strength $|B|$ (nT); B_x, B_y, and B_z (nT) at GSE coordinate system; the number density (cm^{-3}); the plasma temperature (K); and the magnitude of the radial velocity (km/s). The dashed lines denote the measured parameters by ACE: (top to bottom) the magnetic field strength $|B|$ (nT); B_x, B_y, and B_z (nT) at GSE coordinate system; the proton density (cm^{-3}); the proton temperature (K); and the magnitude of the radial velocity (km/s). The solid red vertical line indicates the simulated shock front, and the long-dashed red vertical lines denote the beginning and ending of the MC-like structure.

2005] used the kinematic cone model to simulate the halo-CME event of 12 May 1997 by giving the evolution of plasma parameters, such as the flow velocity, number density, temperature, and magnetic field strength at Earth. *Shen et al.* [2007, 2009] applied the "pressure-driven" model to initialize CME and simulate the halo-CME events of 6 January 1997 and 13 November 2003. These non-flux-rope models reproduced relatively well comparison of the flow parameters, such as the flow velocity, density, and temperature, but often could not well provide the magnetic field structure, especially at 1 AU. *Manchester et al.* [2004b] used an analytical 3-D self-similar flux rope [*Gibson and Low*, 1998] in the streamer belt to mimic the CME and simulate the CME event of 18 October 1998. *Kunkel and Chen* [2010] used an erupting flux rope (EFR) model to simulate a STEREO CME event of 24 December 2007 and gave its 1 AU magnetic field and plasma speed. Their flux rope models [*Manchester et al.*, 2004b; *Kunkel and Chen*, 2010] at 1 AU had nearly identical magnetic magnitude as the observed magnetic cloud with a similar fall of in field strength with time. However, the density by *Manchester et al.* [2004b] was at least two times larger, compared with the observed density, and the flux rope lasted for only 14 h compared with the more than 24 h of the observed cloud.

[33] Presently, all these CME models are candidates for mimicking the morphology near the Sun, with the purpose of reproducing the plasma parameters and the propagation characteristics comparable with 1 AU observation. One reason about the differing degrees of agreement is that our present model, like many others already mentioned, is only a single-fluid (proton) model, which cannot account for the high temperature in the shock of CME and the anticorrelation between the electron temperature and density. More importantly, there exist two other extremely important and still unsolved reasons in many CME models, as pointed out by *Dryer* [1998] and now recognized by some other modelers [*Fry et al.*, 2001; *Odstrcil et al.*, 2004; *Shen et al.*, 2007]. These two reasons are as follows: (1) uncertainty of the initial realistic solar wind and IMF background conditions and (2) uncertainty of the appropriate solar observations used to "mimicking" solar flare/filament and CME initiation. To some extent, our establishment of using more observational data such as magnetic fields and the density by constraining the model is to try to avoid the uncertainty of the initial realistic solar wind. But, the approximate solar observations used to "mimic" solar flare/filament and CME initiation are challenging problems.

[34] It is our belief that more solar and interplanetary observations will clarify these uncertainties. For example, the recently launched Solar Dynamic Observatory (SDO) will help us understand the Sun's magnetic changes. SDO will tell us more about how the magnetic field is generated and structured and how the stored magnetic energy is released into the heliosphere and geospace. STEREO observations can provide new insights into the 3-D structure of CMEs and their evolution in the heliosphere which can directly be compared with existing models and simulations. Comprehensive data and analysis with multiple spacecraft (such as SDO, STEREO, SOHO, ACE, WIND, or other future missions) will probably help us develop the ability of including physically realistic coronal heating modules into

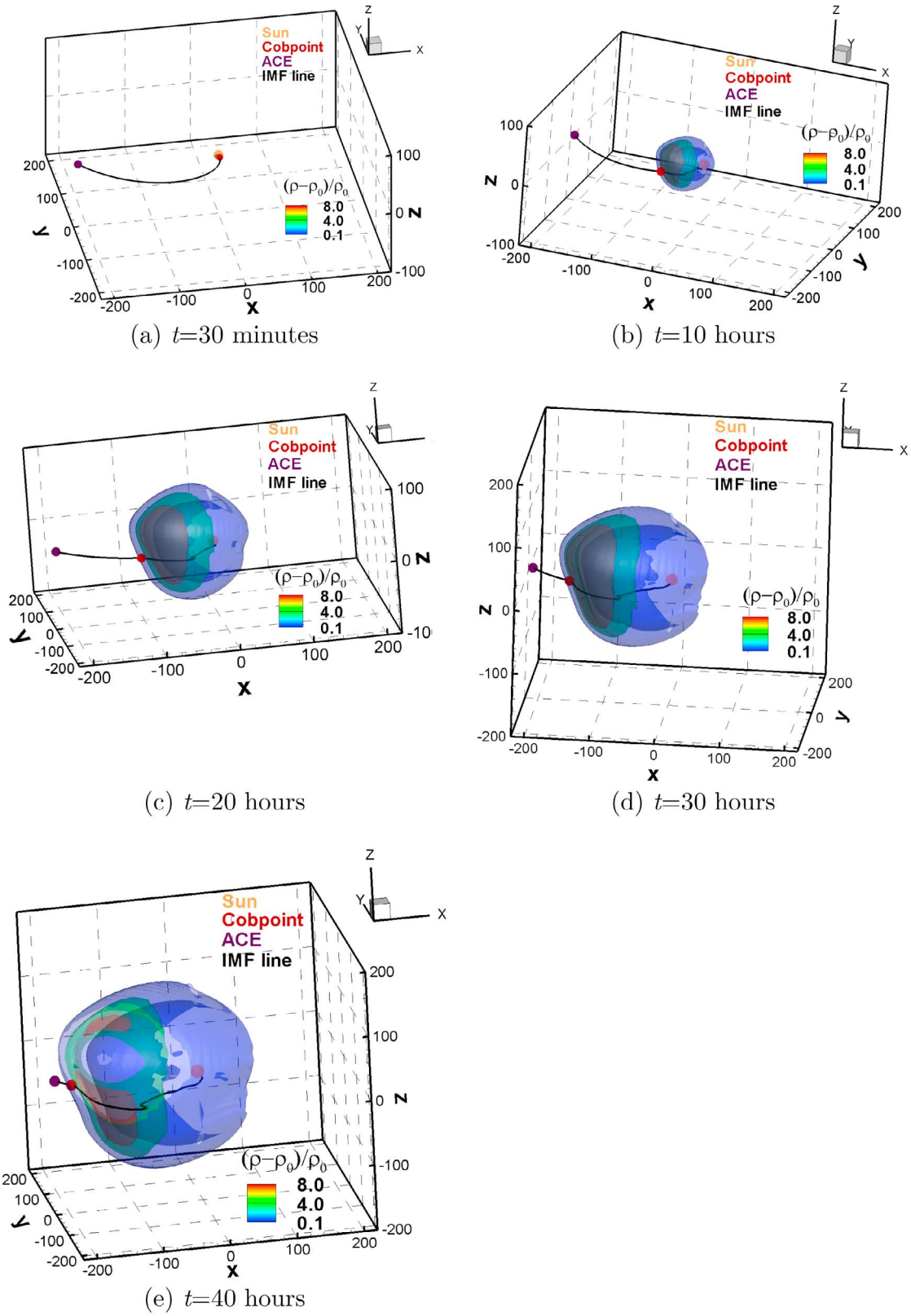

Figure 11. Three-dimensional views of the calculated IMF line (black), the location of the Sun (solid yellow circles), ACE (solid purple circles), and the cobpoint (solid red circles) at (a) t = 30 min, (b) t = 10 h, (c) t = 20 h, (d) t = 30 h, and (e) t = 40 h. The color codes represent isosurfaces of relative density ($(\rho - \rho_0)/\rho_0$) (unit of the axis: R_s).

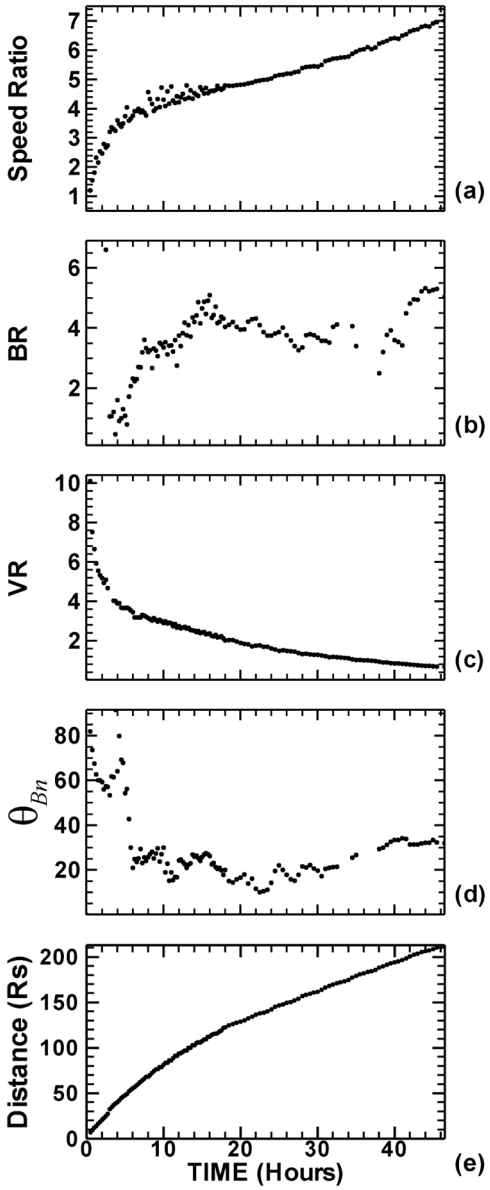

Figure 12. Temporal evolution of (a) the speed ratio, (b) BR, (c) VR, and (d) the θ_{Bn} angle at the cobpoint and (e) the radial distance from the Sun of the cobpoint.

3-D MHD codes, improve the determination of the structure of the ambient solar wind, and further numerically characterize the 3-D propagation of CMEs through the heliosphere, as mentioned by *Feng et al.* [2010].

3.3. Simulation Results of the Cobpoint Located on the Shock Front and Magnetically Connected to the ACE Spacecraft

[35] In order to track the amount of particle flux arrival at L1 point, we especially investigate the evolution of the special point, which is located on the shock front and on the magnetic field line connection between the Sun and ACE at the same time. These points were also called "cobpoints" by some authors [*Heras et al.*, 1995; *Aran et al.*, 2007; *Rodríguez et al.*, 2010], and the simulation of the evolution of the shock strength at these points is an important factor in the combined shock-and-particle acceleration modeling.

[36] The magnetic field line connection between the Sun and ACE can be seen from the MHD simulation discussed in section 3.2. To identify the cobpoint, we use the value of the relative density $\left(\frac{\rho-\rho_o}{\rho_o}\right)$ being 0.1 as the criterion to identify the position of the cobpoint. After the magnetic field line is given, we can obtain the evolution of the cobpoint located on the shock front magnetically connected to the ACE spacecraft at each time. Figure 11 shows 3-D views of the calculated IMF line (black trace), the location of the Sun (yellow solid circle), ACE (purple solid circle), and the cobpoint (red solid circle) at t = 30 min (Figure 11a), t = 10 h (Figure 11b), t = 20 h (Figure 11c), t = 30 h (Figure 11d), and t = 40 h (Figure 11e). The color code of Figure 11 represents the isosurfaces of relative density $\left(\frac{\rho-\rho_o}{\rho_o}\right)$, in which the dark blue isosurface indicates the regions of the CME where the relative density coincides with the criterion value of 0.1. Once these cobpoints are given, in order to compute the plasma jump across the cobpoints, we need to determine the direction of the shock normal $\vec{n}$. Many well-documented existing methods can be used [e.g., *Viñas and Scudder*, 1986; *Szabo*, 1994; *Berdichevsky et al.*, 2000; *Lin et al.*, 2006; *Zuo and Feng*, 2007; *Koval and Szabo*, 2008, and references therein] to determine the shock-normal direction. *Rodríguez et al.* [2010] selected five of them to compare and used the MD3 of the three mixed methods, developed by *Abraham-Shrauner and Yun* [1976]. We also use this MD3 method here to compute the shock normal direction $\vec{n}$:

$$\vec{n} = \pm \frac{\left(\left(\vec{B}_d - \vec{B}_u\right) \times \left(\vec{v}_d - \vec{v}_u\right)\right) \times \left(\vec{B}_u - \vec{B}_d\right)}{\left|\left(\left(\vec{B}_d - \vec{B}_u\right) \times \left(\vec{v}_d - \vec{v}_u\right)\right) \times \left(\vec{B}_u - \vec{B}_d\right)\right|} \tag{7}$$

where the subscripts u and d refer to upstream and downstream values, respectively.

[37] Then, we can estimate the strength of the shock at each time and for every point along the shock front and in particular at the cobpoints. We characterize this strength by the downstream/upstream normalized velocity jump, VR = $(v_{rd} - v_{ru})/v_{ru}$ and the magnetic field ratio, BR = $|B_d|/|B_u|$. The angle between the IMF upstream of the shock and the shock normal, θ_{Bn}, is characterized as quasi-parallelism or quasi-perpendicularity related to the mechanisms of particle acceleration at shocks [*Armstrong et al.*, 1985; *Scholer*, 1985; *Aran*, 2007]. From the shock simulation we will derive the evolution of the parameters VR, BR, and θ_{Bn} at the cobpoint.

[38] The temporal evolution of the speed ratio, BR, VR, and θ_{Bn} at the cobpoint are plotted in Figures 12a to 12d, respectively, and the temporal evolution of the heliocentric distance of the cobpoint (in solar radii) is displayed in Figure 12e. In order to characterize the fluid compressibility, we introduce a speed ratio parameter $V_{\rm tot}/a_s$, where $V_{\rm tot}$ and a_s are the total velocity and the sound speed at the cobpoint, respectively. In Figure 12, the speed ratio increases from >1 to 7 with time, and the magnetic field ratio (BR) also increases with time as a whole, which indicates that both the fluid field and the magnetic field at the cobpoint become more compressed as it expands into the interplanetary medium. In contrast, VR decreases with time, from over

10.0 down to less than 1.0 which is because of the weakening of the shock resulting from its expansion while traveling away from the Sun. The angle between the IMF upstream of the shock and the normal shock front θ_{Bn} drops from near 80° to 20°–30°, which demonstrates that direction of the IMF upstream of the shock and the shock front normal changes from quasi-perpendicularity state to quasi-parallelism state, as the shock expands from near the Sun to the interplanetary space.

[39] By the way, *Manchester et al.* [2005] presented a first attempt discussing the variations of the conditions of the particle acceleration at traveling shocks. Their research presented that the sudden postshock increase in magnetic field strength on low-latitude field lines, which was consistent with our results.

4. Summary and Concluding Remarks

[40] We have used a three-dimensional, time-dependent, numerical MHD model, together with an asynchronous and parallel time-marching method by *Shen et al.* [2009] to investigate large-scale background solar wind structures and the propagation of a specific CME evolution to ICME, with its shock wave in a nonuniform background solar wind flow. This background solar wind is derived from the observed magnetic field and density at the source surface.

[41] Using an asynchronous and parallel time-marching method, we first present the background solar wind from the source surface of 2.5 R_s to the Earth's orbit (215 R_s) and beyond. In this simulation, we apply a self-consistent source surface structure as the initial boundary condition, and the projected normal characteristic method [*Nakagawa et al.*, 1987; *Wu and Wang*, 1987] to deal with the boundary condition at inner boundary. Our numerical results of the background solar wind are qualitatively consistent with observations results given by Ulysses and Helios 2.

[42] We then investigated the dynamical interaction of a CME with the background solar wind flow between 2.5 and 220 R_s. The CME is simulated by means of a high-density, high-velocity, and high-temperature magnetized plasma blob, which is superimposed on a background steady state solar wind with an initial launch direction. We chose the well-defined halo-CME event of 4–6 April 2000 as our test case because of the abundant data available from the SOHO/LASCO and ACE spacecrafts. The choice of the initial parameters about the density, velocity, temperature, and magnetic field are given to match the transit time, the total magnetic field, and other ACE data as the best fit as possible. The numerical simulation results of the 4–6 April 2000 CME propagation are shown in Figures 6 to 9. Figures 6 to 9 clearly show that a shock front with a high velocity and density, and the flux rope is radially compressed. The distorted shock front is due to interaction with the slower solar wind around the heliospheric plasma sheets. The distortion is expected to be greater for larger differences between slow and fast streams.

[43] When the CME evolves to ICME reaching the L1 point, its physical parameters (Figure 10) resembled the observations of the ICME recorded by the ACE spacecraft. Our simulation reproduces some of the in situ measurements: the general shape of the curves is similar, the velocity and temperature display realistic values, and the transit time is approximately reproduced. For the z component of the magnetic field, which is the most important parameter in predicting the intensity of a magnetic storm, the simulated and measured profiles at the L1 point are similar but the MC-like structure in our simulation seems to arrive ~1.5 h earlier than the ACE data and is also smaller than the observed magnetic cloud, especially for the southward magnetic field.

[44] Then, we have performed an analysis of the evolution of the cobpoint for the interests of tracking the amount of particle flux arrival at L1 point. This cobpoint is located at the shock front and its corresponding magnetic field line connection between the Sun and ACE at the same time. It is understood that the simulation of the evolution of the shock strength at the cobpoint is an important factor for the study of SEP events. A first attempt discussing the variations of the conditions of the particle acceleration at traveling shocks was presented by *Manchester et al.* [2005]. We also presented a fully 3-D MHD simulation of the physical shock properties at the cobpoint from the source surface to near the Earth. The numerical results of the propagation of the 3-D magnetic field lines and the location of the cobpoints are shown in Figure 11. The temporal evolution of the speed ratio, the magnetic field ratio (BR), the downstream/upstream normalized velocity jump (VR), the angle between the shock upstream and the shock front normal (θ_{Bn}) at the cobpoint, and the heliocentric distance of the cobpoint are plotted in Figure 12. Figure 12 shows that (1) speed ratio and BR increases as a whole, which indicates that both the fluid field and the magnetic field of the cobpoint become more compressed as it expands into the interplanetary medium; (2) VR decreases with time due to the weakening of the shock from its expansion while traveling away from the Sun; (3) θ_{Bn} drops from near 80° to 20°–30°, which demonstrates that the direction of the IMF upstream of the shock and the shock front normal changes from a quasi-perpendicularity state to a quasi-parallelism state during its propagation from near the Sun to the interplanetary space.

[45] **Acknowledgments.** We are appreciated to the helpful discussion with R. Rodríguez at Universitat de Barcelona, Spain. Here is also mentioned that our cobpoint calculation code referred to the cobpoint code she provided. This work is jointly supported by National Natural Science Foundation of China (40890162, 41031066, 41074121, 40921063, 40874077, 40874091, and 41074122), the Specialized Research Fund for State Key Laboratories and the Ocean Public Welfare Scientific Research Project, State Oceanic Administration People's Republic of China (201005017). S. T. Wu is supported by AFOSR grant FA9550-07-1-0468, NSF grant ATM-0754378, and NSO/AURA grant C-10569A which is a subaward of NSF award 0132798. Special thanks go to our anonymous reviewers for helpful suggestions for the improvement of the paper.

[46] Philippa Browning thanks the reviewers for their assistance in evaluating this paper.

References

Abraham-Shrauner, B., and S. H. Yun (1976), Interplanetary shocks seen by AMES plasma probe on Pioneer 6 and 7, *J. Geophys. Res.*, *81*, 2097–2102.

Aran, A. (2007), Synthesis of proton flux profiles of SEP events associated with interplanetary shocks: The tool SOLPENCO, Ph.D. thesis, Univ. de Barcelona, Barcelona, Spain.

Aran, A., D. Lario, B. Sanahuja, R. G. Marsden, M. Dryer, C. D. Fry, and S. M. P. McKenna-Lawlor (2007), Modeling and forecasting solar energetic particle events at Mars: The event on 6 March 1989, *Astron. Astrophys.*, *469*, 1123–1134, doi:10.1051/0004-6361:20077233.

Armstrong, T. P., M. E. Pesses, and R. B. Decker (1985), *Shock Drift Acceleration*, *Geophys. Monogr. Ser.*, vol. 35, edited by B. T. Tsurutani and R. G. Stone, pp. 271–286, AGU, Washington, D. C.

Berdichevsky, D. B., et al. (2000), Interplanetary fast shocks and associated drivers observed through the 23rd solar minimum by Wind over its first 2.5 years, *J. Geophys. Res.*, *105*, 27,289–27,314.

Burlaga, L. F. (1988), Magnetic clouds and force-free fields with constant alpha, *J. Geophys. Res.*, *93*, 7217–7224, doi:10.1029/JA093iA07p07217.

Burlaga, L. F., E. Sittler, F. Mariani, and R. Schwenn (1981), Magnetic loop behind an interplanetary shock: Voyager, Helios, and IMP 8 observations, *J. Geophys. Res.*, *86*, 6673–6684, doi:10.1029/JA086iA08p06673.

Chané, E., C. Jacobs, B. Van der Holst, S. Poedts, and D. Kimpe (2005), On the effect of the initial magnetic polarity and of the background wind on the evolution of CME shocks, *Astron. Astrophys.*, *432*, 331–339, doi:10.1051/0004-6361:20042005.

Chané, E., B. Van der Holst, C. Jacobs, S. Poedts, and D. Kimpe (2006), Inverse and normal coronal mass ejections: Evolution up to 1 AU, *Astron. Astrophys.*, *447*, 727–733, doi:10.1051/0004-6361:20053802.

Chané, E., S. Poedts, and B. Van der Holst (2008), On the effect of the initial magnetic polarity and of the background wind on the evolution of CME shocks, *Astron. Astrophys.*, *492*, L29–L32.

Chen, J. (1989), Effects of toroidal forces in current loops embedded in a background plasma, *Astrophys. J.*, *338*, 453–470, doi:10.1086/167211.

Chen, J. (1996), Theory of prominence eruption and propagation: Interplanetary consequences, *J. Geophys. Res.*, *101*, 27,499–27,519, doi:10.1029/96JA02644.

Chen, J., and D. A. Garren (1993), Interplanetary magnetic clouds: Topology and driving mechanism, *Geophys. Res. Lett.*, *20*(21), 2319–2322, doi:10.1029/93GL02426.

Chen, J., and V. Kunkel (2010), Temporal and physical connection between coronal mass ejections and flares, *Astrophys. J.*, *717*, 1105–1122.

Detman, T. R., M. Dryer, T. Yeh, S. M. Han, and S. T. Wu (1991), A time-dependent, three-dimensional MHD numerical study of interplanetary magnetic draping around plasmoids in the solar wind, *J. Geophys. Res.*, *96*, 9531–9540, doi:10.1029/91JA00443.

Dryer, M. (1998), Multi-dimensional MHD simulation of solar-generated disturbances: Space weather forecasting of geomagnetic storms, *AIAA J.*, *36*(3), 365–370, doi:10.2514/2.405.

Dryer, M., C. D. Fry, W. Sun, C. S. Deehr, Z. Smith, S.-I. Akasofu, and M. D. Andrews (2001), Prediction in real-time of the 2000 July 14 heliospheric shock wave and its companions during the "Bastille" epoch, *Sol. Phys.*, *204*, 265–284, doi:10.1023/A:1014200719867.

Dryer, M., Z. Smith, C. D. Fry, W. Sun, C. S. Deehr, and S.-I. Akasofu (2004), Real-time shock arrival predictions during the "Halloween 2003 epoch," *Space Weather*, *2*, S09001, doi:10.1029/2004SW000087.

Feng, X., et al. (2003), A class of two-step TVD MacCormack type numerical scheme for MHD equations, *Chin. J. Space Sci.*, *23*, 401–412.

Feng, X., et al. (2005), A comparative study on 3-D solar wind structure observed by Ulysses and MHD simulation, *Chin. Sci. Bull.*, *50*(7), 672–678, doi:10.1360/982004-293.

Feng, X., et al. (2010), Three-dimensional solar wind modeling from the Sun to Earth by a SIP-CESE MHD model with a six-component grid, *Astrophys. J.*, *723*, 300–319, doi:10.1088/0004-637X/723/1/300.

Fry, C. D., W. Sun, C. S. Deehr, M. Dryer, Z. Smith, S.-I. Akasofu, M. Tokumaru, and M. Kojima (2001), Improvements to the HAF solar wind model for space weather predictions, *J. Geophys. Res.*, *106*, 20,985–21,001, doi:10.1029/2000JA000220.

Gibson, S., and B. C. Low (1998), A time-dependent three-dimensional magnetohydrodynamic model of the coronal mass ejection, *Astrophys. J.*, *493*, 460–473, doi:10.1086/305107.

Gosling, J. T. (1990), Coronal mass ejections and magnetic flux ropes in interplanetary space, in *Physics of Magnetic Flux Ropes*, *Geophys. Monogr. Ser.*, vol. 58, edited by E. R. Priest et al., pp. 343–364, AGU, Washington, D. C.

Groth, C. P. T., D. L. De Zeeuw, T. I. Gombosi, and K. G. Powell (2000), Global three-dimensional MHD simulation of a space weather event: CME formation, interplanetary propagation, and interaction with the magnetosphere, *J. Geophys. Res.*, *105*, 25,053–25,078, doi:10.1029/2000JA900093.

Hayashi, K. (2005), Magnetohydrodynamic simulations of the solar corona and solar wind using a boundary treatment to limit solar wind mass flux, *Astrophys. J.*, *161*, 480–494, doi:10.1086/491791.

Heras, A. M., B. Sanahuja, D. Lario, Z. K. Smith, T. Detman, and M. Dryer (1995), Three low-energy particle events: Modeling the influence of the parent interplanetary shock, *Astrophys. J.*, *445*, 497–508, doi:10.1086/175714.

Huttunen, K. E. J., H. E. J. Koskinen, T. I. Pulkkinen, A. Pulkkinen, M. Palmroth, E. G. D. Reeves, and H. J. Singer (2002), April 2000 magnetic storm: Solar wind driver and magnetospheric response, *J. Geophys. Res.*, *107*(A12), 1440, doi:10.1029/2001JA009154.

Jacobs, C., S. Poedts, B. Van der Holst, and E. Chané (2005), On the effect of the background wind on the evolution of interplanetary shock waves, *Astron. Astrophys.*, *430*, 1099–1107, doi:10.1051/0004-6361:20041676.

Jadav, R. M., K. N. Iyer, H. P. Joshi, and H. O. Vats (2005), Coronal mass ejection of 4 April 2000 and associated space weather effects, *Planet. Space Sci.*, *53*(6), 671–679, doi:10.1016/j.pss.2005.01.002.

Koval, A., and A. Szabo (2008), Modified "Rankine-Hugoniot" shock fitting technique: Simultaneous solution for shock normal and speed, *J. Geophys. Res.*, *113*, A10110, doi:10.1029/2008JA013337.

Krall, J., J. Chen, and R. Santoro (2000), Drive mechanisms of erupting solar magnetic flux ropes, *Astrophys. J.*, *539*, 964–982, doi:10.1086/309256.

Krall, J., V. B. Yurchyshyn, S. Slinker, R. M. Skoug, and J. Chen (2006), Flux rope model of the 2003 October 28–30 coronal mass ejection and interplanetary coronal mass ejection, *Astrophys. J.*, *642*, 541–553, doi:10.1086/500822.

Kunkel, V., and J. Chen (2010), Evolution of a coronal mass ejection and its magnetic field in interplanetary space, *Astrophys. J.*, *715*, L80–L83, doi:10.1088/2041-8205/715/2/L80.

Lin, C. C., J. K. Chao, L. C. Lee, L. H. Lyu, and D. J. Wu (2006), A new shock fitting procedure for the MHD Rankine-Hugoniot relations for the case of small He^{2+} slippage, *J. Geophys. Res.*, *111*, A09104, doi:10.1029/2005JA011449.

Linker, J. A., et al. (1999), Magnetohydrodynamic modeling of the solar corona during whole Sun month, *J. Geophys. Res.*, *104*, 9809–9830, doi:10.1029/1998JA900159.

Lugaz, N., and I. I. Roussev (2010), Numerical modeling of interplanetary coronal mass ejections and comparison with heliospheric images, *J. Atmos. Sol. Terr. Phys.*, doi:10.1016/j.jastp.2010.08.016, in press.

Manchester, W. B., et al. (2004a), Three-dimensional MHD simulation of a flux rope driven CME, *J. Geophys. Res.*, *109*, A01102, doi:10.1029/2002JA009672.

Manchester, W. B., et al. (2004b), Modeling a space weather event from the Sun to the Earth: CME generation and interplanetary propagation, *J. Geophys. Res.*, *109*, A02107, doi:10.1029/2003JA010150.

Manchester, W. B., et al. (2005), Coronal mass ejection shock and sheath structures relevant to particle acceleration, *Astrophys. J.*, *622*, 1225–1239, doi:10.1086/427768.

Mariani, F., U. Villante, R. Bruno, B. Bavassano, and N. F. Ness (1979), An extended investigation of HELIOS 1 and 2 observations—The interplanetary magnetic field between 0.3 and 1 AU, *Sol. Phys.*, *63*, 411–421, doi:10.1007/BF00174545.

McComas, D. J., et al. (2000), Solar wind observations over Ulysses' first full polar orbit, *J. Geophys. Res.*, *105*, 10,419–10,433, doi:10.1029/1999JA000383.

McComas, D. J., H. A. Elliott, N. A. Schwadron, J. T. Gosling, R. M. Skoug, and B. E. Goldstein (2003), The three-dimensional solar wind around solar maximum, *Geophys. Res. Lett.*, *30*(10), 1517, doi:10.1029/2003GL017136.

McComas, D. J., H. A. Elliott, J. T. Gosling, and R. M. Skoug (2006), Ulysses observations of very different heliospheric structure during the declining phase of solar activity cycle 23, *Geophys. Res. Lett.*, *33*, L09102, doi:10.1029/2006GL025915.

Nakagawa, Y., Y. Q. Hu, and S. T. Wu (1987), The method of projected characteristics for the evolution of magnetic arches, *Astron. Astrophys.*, *179*, 354–370.

Odstrcil, D., and V. J. Pizzo (1999a), Three-dimensional propagation of coronal mass ejections (CMEs) in a structured solar wind flow: 1. CME launched within the streamer belt, *J. Geophys. Res.*, *104*, 483–492, doi:10.1029/1998JA900019.

Odstrcil, D., and V. J. Pizzo (1999b), Distortion of the interplanetary magnetic field by three-dimensional propagation of coronal mass ejections in a structured solar wind, *J. Geophys. Res.*, *104*, 28,225–28,239, doi:10.1029/1999JA900319.

Odstrcil, D., M. Dryer, and Z. Smith (1996), Propagation of an interplanetary shock along the heliospheric plasma sheet, *J. Geophys. Res.*, *101*, 19,973–19,986, doi:10.1029/96JA00479.

Odstrcil, D., J. A. Linker, R. Lionello, Z. Mikic, P. Riley, V. J. Pizzo, and J. G. Luhmann (2002), Merging of coronal and heliospheric numerical 2-D MHD models, *J. Geophys. Res.*, *107*(A12), 1493, doi:10.1029/2002JA009334.

Odstrcil, D., et al. (2003), 3-D simulations of ICMEs by coupled coronal and heliospheric models, in *Solar Variability as an Input to the Earth's Environment*, *Eur. Space Agency Spec. Publ.*, *ESA SP-535*, pp. 541–546, Eur. Space Agency, Noordwijk, Netherlands.

Odstrcil, D., P. Riley, and X. P. Zhao (2004), Numerical simulation of the 12 May 1997 interplanetary CME event, *J. Geophys. Res.*, *109*, A02116, doi:10.1029/2003JA010135.

Odstrcil, D., V. J. Pizzo, and C. N. Arge (2005), Propagation of the 12 May 1997 interplanetary coronal mass ejection in evolving solar wind structures, *J. Geophys. Res.*, *110*, A02106, doi:10.1029/2004JA010745.

Owens, M. J., H. E. Spence, S. McGregor, W. J. Hughes, J. M. Quinn, C. N. Arge, P. Riley, J. Linker, and D. Odstrcil (2008), Metrics for solar wind prediction models: Comparison of empirical, hybrid, and physics-based schemes with 8 years of L1 observations, *Space Weather*, *6*, S08001, doi:10.1029/2007SW000380.

Plunkett, S. P., and S. T. Wu (2000), Coronal mass ejections (CMEs) and their geoeffectiveness, *IEEE Trans. Plasma Sci.*, *28*(6), 1807–1817, doi:10.1109/27.902210.

Riley, P., J. A. Linker, and Z. Mikic (2001), An empirically driven global MHD model of the solar corona and inner heliosphere, *J. Geophys. Res.*, *106*, 15,889–15,901, doi:10.1029/2000JA000121.

Riley, P., J. A. Linker, Z. Mikic, D. Odstrcil, V. J. Pizzo, and D. F. Webb (2002), Evidence of post eruption reconnection associated with coronal mass ejections in the solar wind, *Astrophys. J.*, *578*, 972–978, doi:10.1086/342608.

Riley, P., J. A. Linker, Z. Mikic, and D. Odstrcil (2004), Magnetohydrodynamic modeling of interplanetary CMEs, *IEEE Trans. Plasma Sci.*, *32*(4), 1415–1424, doi:10.1109/TPS.2004.833397.

Rodríguez, R., et al. (2009), Three frontside full halo coronal mass ejections with a nontypical geomagnetic response, *Space Weather*, *7*, S06003, doi:10.1029/2008SW000453.

Rodríguez, R., A. Aran, B. Sanahuja, C. Jacobs, and S. Poedts (2010), Why should the latitude of the observer be considered when modeling gradual proton events?: An insight using the concept of cobpoint, *Adv. Space Res.*, doi:10.1016/j.asr.2010.03.021, in press.

Roussev, I. I., et al. (2003), A three-dimensional flux rope model for coronal mass ejections based on a loss of equilibrium, *Astrophys. J.*, *588*, L45–L48, doi:10.1086/375442.

Scholer, M. (1985), *Diffusive Acceleration*, *Geophys. Monogr. Ser.*, vol. 35, edited by B. T. Tsurutani and R. G. Stone, pp. 287–301, AGU, Washington, D. C.

Shen, F., X. Feng, S. T. Wu, and C. Xiang (2007), Three-dimensional MHD simulation of CMEs in three-dimensional background solar wind with the self-consistent structure on the source surface as input: Numerical simulation of the January 1997 Sun-Earth connection event, *J. Geophys. Res.*, *112*, A06109, doi:10.1029/2006JA012164.

Shen, F., X. Feng, and W. B. Song (2009), An asynchronous and parallel time-marching method: Application to the three-dimensional MHD simulation of the solar wind, *Sci. Chin. Ser. E Technol. Sci.*, *52*(10), 2895–2902.

Shen, F., X. Feng, C. Xiang, and W. B. Song (2010), The statistical and numerical study of the global distribution of coronal plasma and magnetic field near 2.5 Rs over a 10-year period, *J. Atmos. Sol. Terr. Phys.*, *72*, 1008–1018, doi:10.1016/j.jastp.2010.05.016.

Szabo, A. (1994), An improved solution to the "Rankine-Hugoniot" problem, *J. Geophys. Res.*, *99*, 14,737–14,746.

Titov, V. S., and P. Démoulin (1999), Basic topology of twisted magnetic configurations in solar flares, *Astron. Astrophys.*, *351*, 707–720.

Tóth, G. (2000), The $\nabla \cdot \vec{B} = 0$ constraint in shock-capturing magnetohydrodynamics codes, *J. Comput. Phys.*, *161*, 605–652.

Usmanov, A. V., M. L. Goldstein, B. P. Besser, and J. M. Frizel (2000), A global MHD solar wind model with WKB Alfvén waves: Comparison with Ulysses data, *J. Geophys. Res.*, *105*, 12,675–12,695, doi:10.1029/1999JA000233.

Viñas, A. F., and J. D. Scudder (1986), Fast and optimal solution to the "Rankine-Hugoniot problem," *J. Geophys. Res.*, *91*, 39–58.

Wei, F. S., X. S. Feng, H. C. Cai, and Q. J. Zhou (2003), Global distribution of coronal mass outputs and its relation to solar magnetic field structures, *J. Geophys. Res.*, *108*(A6), 1238, doi:10.1029/2002JA009439.

Wu, C.-C., and R. P. Lepping (2005), Relationships for predicting magnetic cloud-related geomagnetic storm intensity, *J. Atmos. Sol. Terr. Phys.*, *67*, 283–291, doi:10.1016/j.jastp.2004.07.040.

Wu, S. T., and J. F. Wang (1987), Numerical tests of a modified full implicit Eulerian scheme with projected normal characteristic boundary conditions for MHD flows, *J. Comp. Meth. Appl. Mech. Eng.*, *24*, 267–282.

Wu, S. T., W. P. Guo, and M. Dryer (1997), Dynamical evolution of a coronal streamer-flux rope system: II. A self-consistent non-planar magnetohydrodynamic solution, *Sol. Phys.*, *170*, 265–282, doi:10.1023/A:1004954816406.

Wu, S. T., W. P. Guo, D. J. Michels, and L. F. Burlaga (1999), MHD description of the dynamical relationships between a flux rope, streamer, coronal mass ejection, and magnetic cloud: An analysis of the January 1997 Sun-Earth connection event, *J. Geophys. Res.*, *104*, 14,789–14,801, doi:10.1029/1999JA900099.

Wu, S. T., T. X. Zhang, E. Tandberg-Hanssen, Y. Liu, X. Feng, and A. Tan (2004), Numerical magnetohydrodynamic experiments for testing the physical mechanisms of coronal mass ejections acceleration, *Sol. Phys.*, *225*, 157–175, doi:10.1007/s11207-004-2568-7.

Wu, S. T., A. H. Wang, Y. Liu, and J. T. Hoeksema (2006), Data-driven magnetohydrodynamic model for active region evolution, *Astrophys. J.*, *652*, 800–811, doi:10.1086/507864.

Xiang, C. Q., X. S. Feng, Q. L. Fan, and J. S. Yao (2006), An observation-based model of solar wind background, *Chin. J. Space Sci.*, *26*, 161–166.

Zhou, Y. F., X. Feng, and S. T. Wu (2008), Numerical simulation of the 12 May 1997 CME event, *Chin. Phys. Lett.*, *25*, 790–793, doi:10.1088/0256-307X/25/2/119.

Zuo, P. B., and X. Feng (2007), The plasma and magnetic field characteristics of a double discontinuity in interplanetary space, *Sol. Phys.*, *240*, 347–357, doi:10.1007/s11207-007-0278-7.

X. S. Feng, F. Shen, W. B. Song, and C. Q. Xiang, SIGMA Weather Group, State Key Laboratory of Space Weather, Center for Space Science and Applied Research, Chinese Academy of Sciences, 1 Nanertiao, Zhongguancun, Beijing 100190, China. (fshen@spaceweather.ac.cn)

S. T. Wu, Center for Space Plasma and Aeronomic Research, University of Alabama in Huntsville, Huntsville, AL 35899, USA.